

Visualizing kinetic pathways of homogeneous nucleation in colloidal crystallization

Peng Tan¹, Ning Xu² and Lei Xu¹

1. Department of Physics, The Chinese University of Hong Kong, Hong Kong, China

*2. Hefei National Laboratory for Physical Sciences at the Microscale,
and CAS Key Laboratory of Soft Matter Chemistry, and Department of Physics,
University of Science and Technology of China, Hefei, China*

(Dated: November 20, 2013)

I. Experimental Details and Phase Diagram

To prepare the soft-repulsive systems, we suspend NBD dyed poly(methyl methacrylate) (PMMA) colloids in a mixture of the non-polar solvent (tetrahydronaphthalene, Aldrich) and the weakly-polar solvent (mixture of Iododecane and Iodododecane, Aldrich) inside a glass capillary. The volume ratio between the non-polar and weakly polar solvents are varied from 1:2 to 1:8, which results in suspensions with conductivity ranging from 100pS/cm to 1nS/cm. The volume ratio between the two weakly polar solvents, Iododecane and Iodododecane, is adjusted from 2:1 to 4:1, to make sure an excellent density match between the solvent and particles. To avoid surface nucleation, the glass walls are coated with one layer of randomly packed particles. The colloids have the diameter $\sigma = 2.2\mu\text{m}$ with the polydispersity less than 2.5%. They are purchased from Edinburgh Research and Innovation Ltd. (see the detailed information at <http://www2.ph.ed.ac.uk/~abs/>). The solvent closely matches both the refractive index and the density of particles. The particles are grafted with polyhydroxystearic acid polymers negatively charged in the solvent and interact with each other via weakly screened electric repulsion (hard-core Yukawa potential), which leads to the formation of Wigner crystal at low concentrations¹⁻³. We fix the concentration at 17% to avoid the hard-core direct contacts among particles.

By varying the relative fractions between non-polar and weakly polar solvents, we can adjust the Debye screening length, κ^{-1} , and the surface charge, Z , to tune the stable solid state^{2,4}. The phase diagram is established from the measurements of various samples, as shown in Fig.SI-1A. To compare with the previous phase diagram⁴, we use the variables of λ and U_0 which are calculated from the screening length and the surface charge: $\lambda = \kappa\sigma/(6\phi/\pi)^{-1/3}$, $U_0 = e^{\kappa\sigma}\epsilon(6\phi/\pi)^{1/3}$. Here σ is the particle diameter, κ^{-1} is the screening length, ϕ is the volume fraction, $\epsilon = Z^2e^2/4\pi\epsilon_s[\sigma(1 + \kappa\sigma/2)^2]$, with ϵ_s being the dielectric constant of the solvent. The symbols are from our measurements and the solid lines are from the previous simulation⁴. The two sets of values agree well. The two arrows indicate the locations of the two systems (BCC-stable and FCC-stable respectively) shown in the main text. To have a more complete picture, we have also varied the volume fraction of the samples.

The phase diagram is obtained by quantitative measurements on the screening length, κ^{-1} , and the surface charge number, Z , as shown in Fig.SI-1B. We obtain the screening

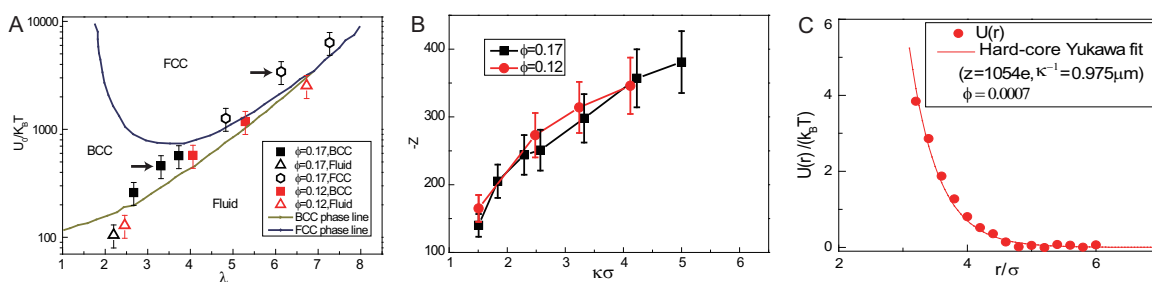


FIG. SI- 1: The phase diagram of our systems. **A**, phase diagram as the function of λ and U_0 . Here $\lambda = \kappa\sigma/(6\phi/\pi)^{-1/3}$ and $U_0 = e^{\kappa\sigma}\epsilon(6\phi/\pi)^{1/3}$. σ is the particle diameter, κ^{-1} is the screening length, ϕ is the volume fraction, $\epsilon = Z^2 e^2 / 4\pi\epsilon_s [\sigma(1 + \kappa\sigma/2)^2]$, with ϵ_s being the dielectric constant of the solvent. The symbols are from our measurements and the solid lines are from the previous simulation⁴. The two sets of values agree well. The two arrows indicate the locations of the two systems (BCC-stable and FCC-stable respectively) shown in the main text. Two volume fractions, $\phi = 12\%$ and $\phi = 17\%$, are measured. **B**, measurements of the screening length, κ^{-1} , and the surface charge number, Z . **C**, the pair potential between two particles measured at very low volume fraction, $\phi = 0.0007$. Our data is consistent with the hard-core Yukawa potential, as indicated by the solid line. The surface charge $Z = -1054e$ and the screening length $\kappa^{-1} = 0.975\mu m$ are obtained from fitting.

length from conductivity measurements as the following: first we measure the conductivity of the suspension in a $1\text{cm} \times 1\text{cm} \times 5\text{cm}$ cell, and then acquire the conductivity of the solvent with the Maxwell-Garnett Theory⁵; the screening length is then obtained from the conductivity data from the Walden's rule^{6,7}, which gives the molar conductivity of the ions in the solvent. The surface charge, Z , is measured from electrophoresis⁸. Inside a rectangular capillary ($0.12\text{mm} \times 2\text{mm} \times 2.5\text{cm}$), we measure the mobility of particles driven by an AC electric field ($V_{pp} = 10\text{V}$, $f = 0.05\text{Hz}$) between two parallel platinum wires (diameter 0.076mm , Aldrich). The zeta potential is calculated from mobility⁹, and the surface charge is obtained from the empirical relation proposed by Loeb *et al*¹⁰. We have also measured the pair potential between two particles in a dilute sample with volume fraction $\phi = 0.0007$. The potential is consistent with the hard-core Yukawa potential, as shown in Fig.SI-1C. The surface charge $Z = -1054e$ and the screening length $\kappa^{-1} = 0.975\mu m$ are obtained from fitting. The surface charge Z is also separately obtained from the Zeta potential measurements ($Z = -1075e$, zeta potential= -110mV , ZetaPLUS, Brookhaven),

and is consistent with the data from Fig.SI-1C.

We shear melt colloidal crystals with a magnetic wire driven by a magnet and record the re-crystallization process immediately after agitation, with a Leica SP5 confocal microscope. After agitation stops, the flow in the capillary ceases within a few tens of seconds, and the subsequent recrystallization occurs on the time scale of several hours to a few tens of hours. We use image-processing¹¹ to determine the 3D positions of all colloidal particles in each imaging stack. A typical imaging stack has the $x \times y \times z$ dimensions of $110 \times 110 \times 100 \mu m^3$ and contains about 40000 particles. The scanning speeds in all dimensions are at least 30 times faster than the particle free diffusion, which enables the precise locating of particles. We typically collect data over 40 to 50 stacks in each sample for a good statistics. We estimate the degree of supercooling, ΔT , below the melting temperature, T_m , for the various solid samples in the phase diagram (Fig.SI-1A). Two different approaches are applied: the distance from the melting line yields $\Delta T = 0.2T_m \sim 0.44T_m$; and the Lindemann parameter approach^{12,13} gives $\Delta T = 0.2T_m \sim 0.4T_m$. The two independent estimations agree with each other within the experimental accuracy.

II. Local Bond Order Analysis

A. Previous Method

The local bond order parameters are first introduced by Steinhardt *et. al*¹⁴, and Ten Wolde *et al.*¹⁵ used them to identify the nuclei from liquid background. To measure the local bond order parameters for any particle i , a list of neighbors is first determined by finding all particles within a distance r_c from the particle. r_c is typically determined from the first minimum of the radial distribution function $g(r)$. The total number of neighbors is denoted as $Nb(i)$. A bond orientational order parameter $q_l(i)$ is then defined for this particle i as: $q_l(i) = (\frac{4\pi}{2l+1} \sum_{m=-l}^l |q_{l,m}(i)|^2)^{1/2}$, with $q_{l,m}(i) = \frac{1}{Nb(i)} \sum_{j=1}^{Nb(i)} Y_{l,m}(\theta_{i,j}, \phi_{i,j})$. Here $Y_{l,m}(\theta_{i,j}, \phi_{i,j})$ are the spherical harmonics with $m \in [-l, l]$. $\theta_{i,j}$ and $\phi_{i,j}$ are the polar and azimuthal angles of the vector $\mathbf{r}_{ij} = \mathbf{r}_i - \mathbf{r}_j$ with \mathbf{r}_i the position vector of particle i and \mathbf{r}_j the position vector of any neighboring particle j .

$q_l(i)$ can further be coarse grained over all neighbors to obtain $\bar{q}_l(i)$ ¹⁶: $\bar{q}_l(i) = (\frac{4\pi}{2l+1} \sum_{m=-l}^l |\bar{q}_{l,m}(i)|^2)^{1/2}$, with $\bar{q}_{l,m}(i) = \frac{1}{Nc(i)+1} \sum_{j=0}^{Nc(i)} q_{l,m}(j)$. Here the sum from $j = 0$ to

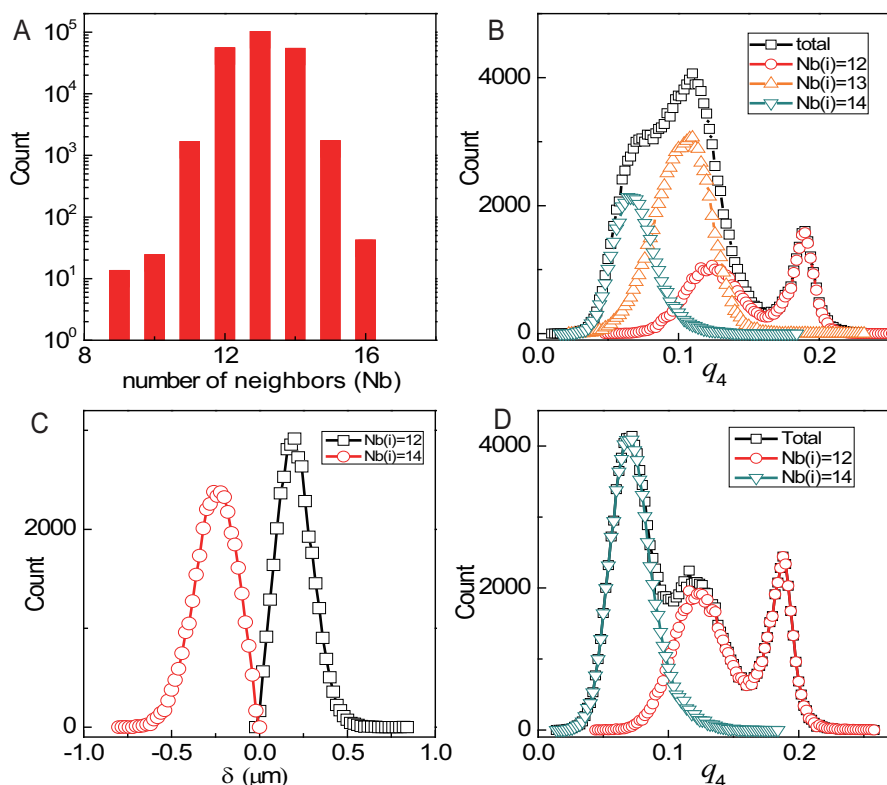


FIG. SI- 2: **Categorizing the 13-neighbor particles.** **A**, number distribution of solid particles with different neighbors. The particles with 12, 13 and 14 neighbors dominate. **B**, the distribution of $q_4(i)$ for all particles shown in **A**. The peak for the 14-neighbor particles corresponds to the BCC symmetry, and the two peaks for the 12-neighbor particles correspond to HCP and FCC symmetries. The 13-neighbor particles do not correspond to any crystalline structure. **C**, Using the quantity $\delta = \frac{r_{13}+r_{14}}{2} - r_c$, we can categorize the 13-neighbor particles back into the 12-neighbor and the 14-neighbor branches. **D**, the new approach gives three sharp peaks in the q_4 distribution which correspond to BCC, HCP and FCC structures respectively.

$Nc(i)$ runs over the particle i itself plus the neighbor particles which are in the same phase (liquid or solid) as the particle i ($Nc(i) \leq Nb(i)$)¹⁷. This treatment avoids the spatial average over particles of different phases, and thus provides a more precise characterization for the coarse grained local structure .

Another set of bond order parameters, $W_l(i) = \sum_{m_1, m_2, m_3=0}^l \binom{l}{m_1} \binom{l}{m_2} \binom{l}{m_3} \frac{q_{l, m_1}(i) q_{l, m_2}(i) q_{l, m_3}(i)}{|q_l(i)|^3}$, are also used in this paper. The parentheses term is the Wigner $3j$ symbol, which is different from zero only for $m_1 + m_2 + m_3 = 0$

¹⁴. W_l is rotational invariant and useful to distinguish different crystalline polymorph such as BCC, HCP and FCC.

When two neighboring particles have very similar local environment, they are said to be connected with one solid bond. The solid bond number for any particle i is defined as: $\xi(i) = \sum_{j=1}^{Nb(i)} (H(d_l(i, j) - d_c))$, with H being the Heaviside step function, $d_c = 0.7$ being the cutoff value, and $d_l(i, j) = \frac{\sum_{m=-l}^l q_{l,m}(i) q_{l,m}^*(j)}{(\sum_{m=-l}^l |q_{l,m}(i)|^2)^{1/2} (\sum_{m=-l}^l |q_{l,m}(j)|^2)^{1/2}}$ quantifying the similarity of local environment between particle i and particle j ¹⁸. Particle i is defined as a solid particle if $\xi(i) \geq \xi_c$, with $\xi_c = 7$ being the typical boundary between liquid and solid. Precursors are identified as the particles with $\xi(i) < \xi_c$ but $\bar{q}_6(i) > 0.27$, which means that they are liquid structures but have relatively-high local bond order¹⁹.

We first use the previous method to analyze our solid particles ($\xi(i) \geq 7$), as shown in Fig.SI-2A and Fig.SI-2B. Fig.SI-2A shows the statistics on the number of neighbors within the first minimum of $g(r)$, for all solid particles in a randomly selected sample (different from the sample in the main text). Clearly, particles with 12, 13 and 14 neighbors dominate (> 98%) while other components are negligible. We therefore focus on these three types of particles only. The particles with HCP and FCC symmetries have 12 neighbors; and the ones with BCC symmetry have 14 neighbors. However, no crystalline structure has 13 neighbors. These results are clearly demonstrated by the statistics on q_4 in Fig.SI-2B. The single peak in the 14-neighbor branch corresponds to the BCC-symmetry; and the two peaks in the 12-neighbor branch correspond respectively with HCP and FCC structures. The peak of the 13-neighbor particles, however, does not correspond to any crystalline structure. To deal with these significant amount of 13-neighbor particles, we develop a new approach as described below.

B. Our Approach

We believe the origin of most 13-neighbor particles is still the 12-neighbor (HCP or FCC) or the 14-neighbor (BCC) ones, with local bond orders deformed by thermal fluctuations. However, the deformations are typically small and most 13-neighbor structures are either closer to a 12-neighbor structure or to a 14-neighbor one. Based on this property, we categorize 13-neighbor particles back into either the 12-neighbor or the 14-neighbor branch, which do have corresponding crystalline structures. We use the quantity $\delta = (r_{13} + r_{14})/2 - r_c$

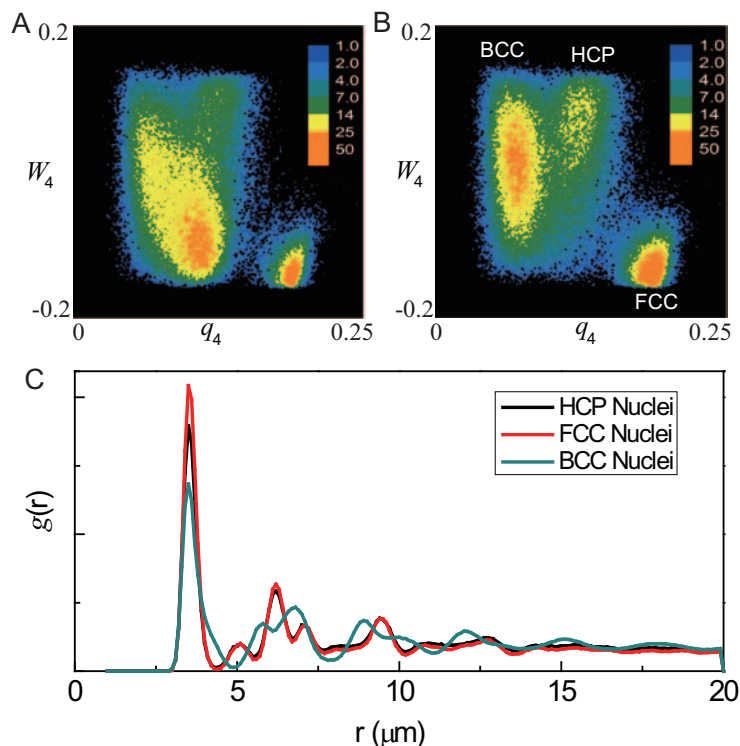


FIG. SI- 3: **A better structure distinction from our approach.** **A**, number distribution in the $W_4 - q_4$ plane using previous method. The BCC and HCP structures are heavily mixed due to the 13-neighbor particles. **B**, our approach achieves a good separation for all three structures. **C**, $g(r)$ for the three types of structures obtained from our approach. The peak locations match the ideal crystals reasonably well.

to categorize the 13-neighbor particles as shown in Fig.SI-2C. Here r_{13} and r_{14} are the distances of the 13th and 14th nearest neighbors. For a normal BCC-symmetry particle, the 13th and 14th neighbors are within the first minimum of $g(r)$ (i.e., r_c). A thermal deviation may move the 14th neighbor slightly out of r_c to form a 13-neighbor structure, but the average distance over the 13th and the 14th neighbors are most likely still less than r_c ($\delta < 0$). Similarly, for a particle with FCC or HCP-symmetry, normally both the 13th and the 14th nearest particles are out of r_c . The thermal deviation may move the 13th particle slightly inside r_c to form a 13-neighbor structure but the average distance over the 13th and the 14th particles is most likely still larger than r_c ($\delta > 0$). The effective separation in Fig.SI-2C demonstrates the robustness of our approach.

Consequently we analyze our nuclei particles with the following procedure: for any particle i , if it has $Nb(i) = 12$ or $Nb(i) = 14$, we do nothing; if it has $Nb(i) = 13$, we set $Nb(i)$

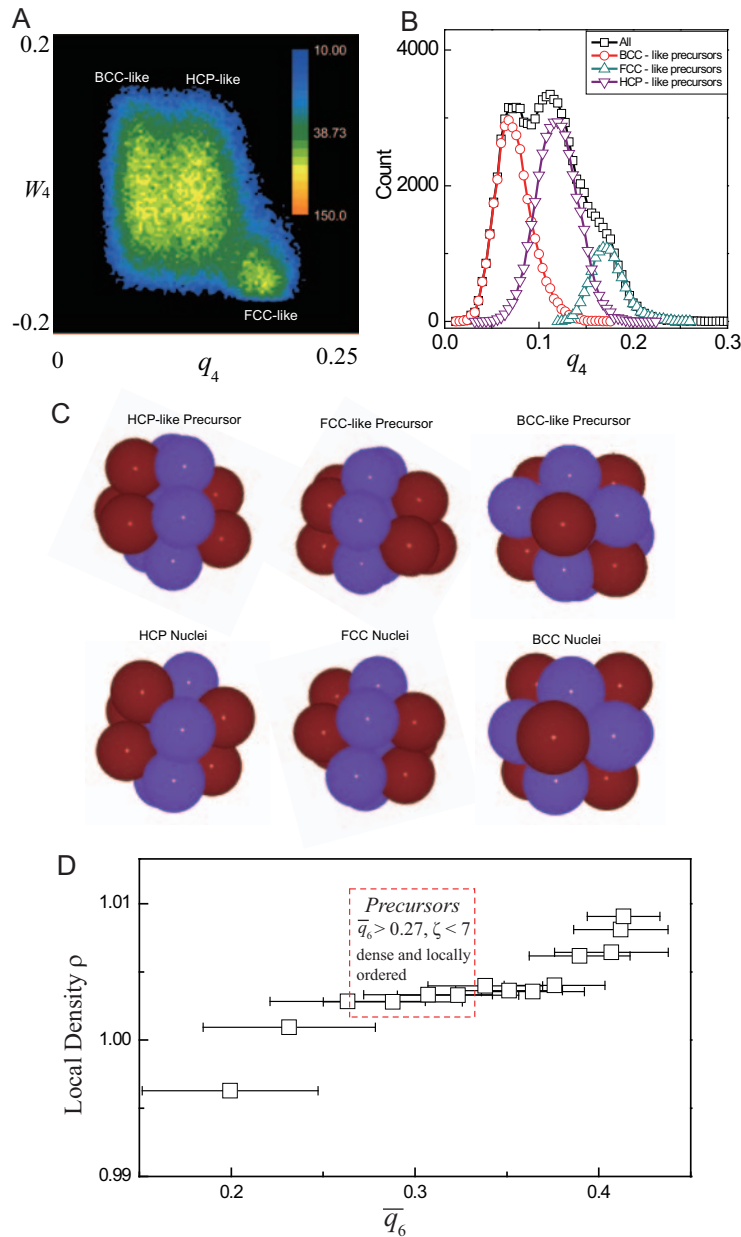


FIG. SI- 4: **Analyzing precursors with our approach.** **A**, three types of precursors are identified in the $W_4 - q_4$ plane, which have good correspondence with the nuclei structures in Fig.SI-3B. **B**, the three structures directly extracted from **A** produce three sharp peaks in the q_4 distribution. They add up to reach the total distribution very nicely, without any fitting. **C**, similar local structures between precursors and nuclei are observed in experiments. The purple spheres are hexagonally packed particles for HCP and FCC symmetries; and eight corner particles for BCC symmetry. **D**, the density of precursors (the box region) is higher than the normal liquid (the region left to the box), but less than the nuclei (the region right to the box).

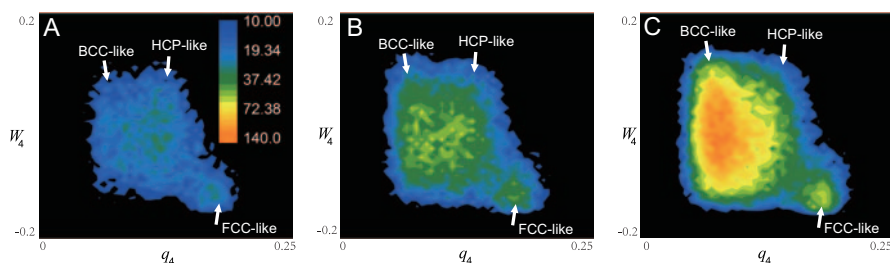


FIG. SI- 5: **Time evolution of precursors in a BCC-stable system.** At the beginning (A, $\phi_{nuclei}=0.019$, $\phi_{precursor}=0.056$, $t=240s$), HCP-like symmetry dominates. Around the critical stage (B, $\phi_{nuclei}=0.071$, $\phi_{precursor}=0.116$, $t=2640s$), BCC-like symmetry catches up. In the post-critical stage (C, $\phi_{nuclei}=0.214$, $\phi_{precursor}=0.204$, $t=6480s$), BCC-like symmetry dominates.

to 12 for $\delta > 0$ or 14 for $\delta < 0$. This procedure effectively eliminates the 13-neighbor particles and divide almost all particles into two branches: the 12-neighbor or the 14-neighbor branch. The two branches are unambiguously composed by BCC, HCP and FCC symmetries, as demonstrated by the three sharp peaks in Fig.SI-2D. The power of our approach is further illustrated by the particle number distribution in the $W_4 - q_4$ plane: Fig.SI-3A comes from the previous method whose BCC and HCP structures are heavily mixed due to the 13-neighbor particles; while our approach in Fig.SI-3B yields a clear distinction for all three structures, which correspond to BCC, HCP and FCC symmetries respectively^{20,21}. Fig.SI-3C shows the $g(r)$ functions for the three crystalline structures calculated with our technique, whose peak locations have good correspondence with the ideal structures.

With exactly the same procedure used for solid particles, we can also analyze the precursor particles in the liquid stage, as shown in Fig.SI-4 (as well as in Fig.1F of main text). From Fig.SI-4A, we can clearly identify three types of precursors: BCC-like, HCP-like and FCC-like ones. The three types of precursors exacted directly from Fig.SI-4A produce three sharp peaks in the q_4 distribution in Fig.SI-4B, and add up to reach the total distribution very nicely. Thus our approach achieves direct structure separation in the $W_4 - q_4$ plane and avoids the method of fitting from total distribution previously employed²¹. The precursors and corresponding nuclei are observed to have similar local structures, as demonstrated by Fig.SI-4C. They also have densities higher than normal liquid but lower than nuclei, as shown in Fig.SI-4D.

The time evolution of precursors is shown in Fig.SI-5. In a BCC-stable system, the

precursors are initially dominated by HCP-like symmetry (image A); while the BCC-like symmetry catches up around the critical stage (image B), and eventually takes over in the post-critical stage (image C). This symmetry transformation is consistent with the description in the maintext: there is a major cross-symmetry pathway from HCP symmetry to BCC symmetry.

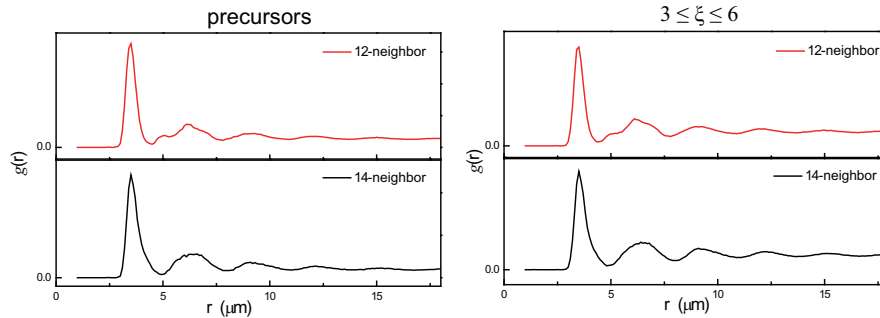


FIG. SI- 6: **Similarity between precursors and the particles with $3 \leq \xi \leq 6$.** The almost identical $g(r)$ functions suggest that the two should have a large overlap.

We also find that the precursors and the particles with $3 \leq \xi \leq 6$ largely overlap with each other, as demonstrated by the almost identical $g(r)$ functions in Fig.SI-6.

C. The Comparison Between Our Approach and the Previous Method

We further compare the our approach with the previous method by analyzing more bond order parameters, as show in Fig.SI-7. In the $q_4 - q_8$ plane, we can see clear symmetry differentiation for both nuclei and precursors with our approach (the top row); while the previous method does not distinguish them as nicely (the bottom row).

Moreover, we must clarify one important point: the local order of precursors we talked about is quite short-ranged, typically extending only to the first shell (the central particle plus its 12 or 14 neighbors). When the coarse grained bond order parameters that involve a longer range (the 1st and 2nd shells) are considered ($\bar{q}_4 - \bar{q}_8$ map for example), the result is quite different. As plotted in Fig.SI-8, the $\bar{q}_4 - \bar{q}_8$ map from our approach is almost identical to the previous method, demonstrating no clear symmetry differentiation at this longer range. This is due to the following reason: the bulk phase of precursors is a mixture of various components with different local symmetries, and therefore lacks the translational

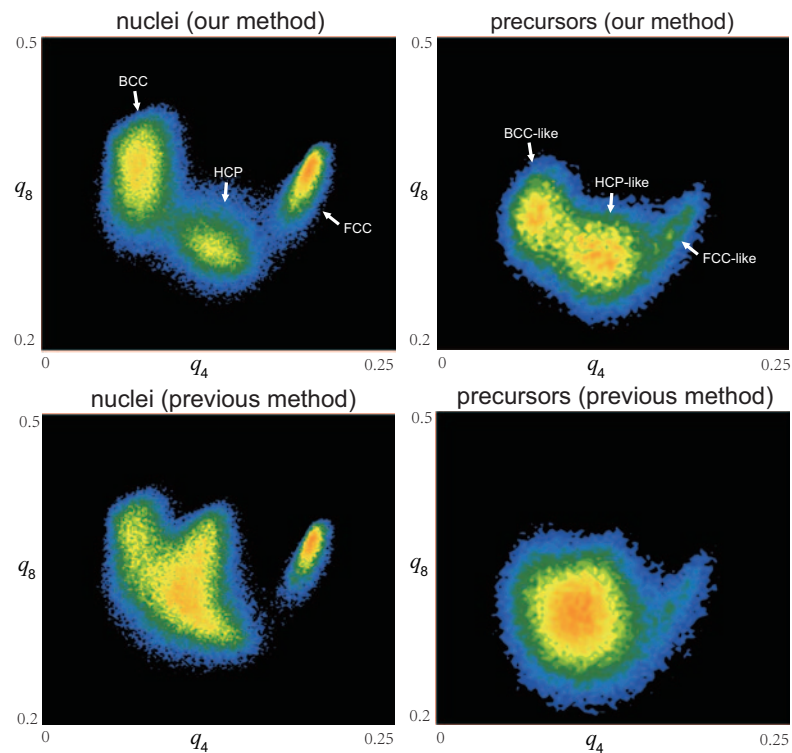


FIG. SI- 7: **Comparison between two approaches in the $q_4 - q_8$ plane.** Clearly our approach (top row) distinguishes different symmetries better than the previous method (bottom row).

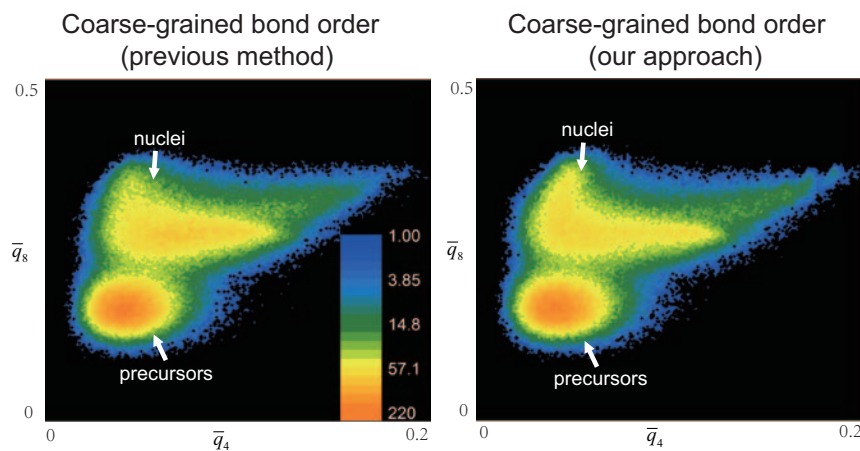


FIG. SI- 8: **Comparison between two approaches in the $\bar{q}_4 - \bar{q}_8$ plane.** The two approaches are very similar in this coarse grained order parameter plane, indicating that the symmetry found in precursors are only short ranged.

coherence and can not be considered as bulk crystal-like. Therefore, we emphasize that our precursors have local order at short range but are still amorphous at the medium-range and

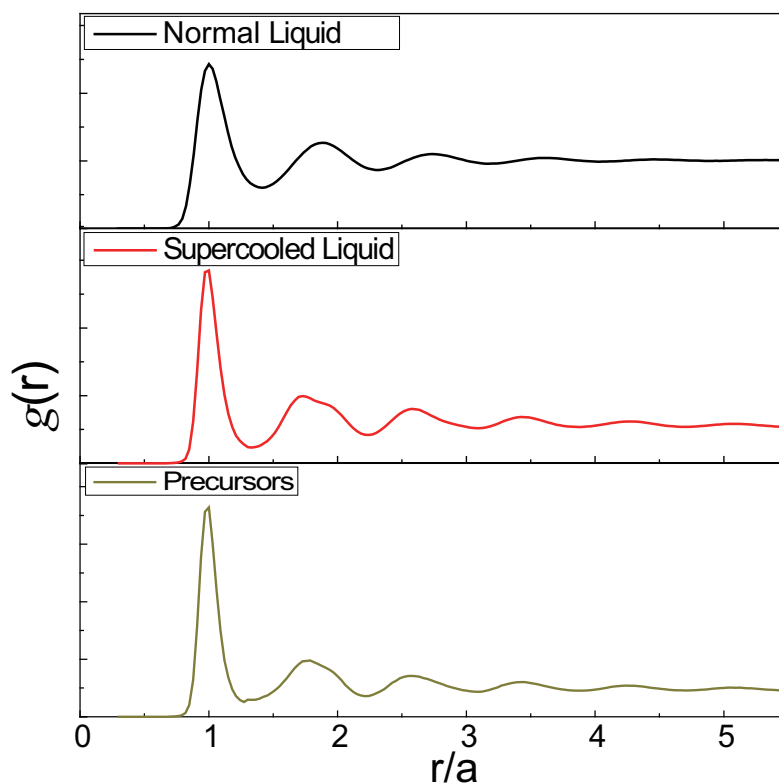


FIG. SI- 9: $g(r)$ for normal liquid ($T > T_m$), supercooled liquid ($T < T_m$) and precursors. These $g(r)$ functions indicate amorphous structures at the bulk level.

at the bulk level. In the previous studies^{22–25} the order is mainly quantified with \bar{q}_l or $g(r)$ at medium range or bulk level, and therefore the conclusion of amorphous precursors is obtained. Our results at these levels (i.e., \bar{q}_l or $g(r)$) are consistent with previous studies; however with the new approach we can also reveal multiple local orders at the short-range level.

To have a better understanding of the precursor structure at the bulk level, we plot the pair correlation function, $g(r)$, in Fig.SI-9. Unlike the $g(r)$ plotted in the main text (Fig.1H), which is from the particles picked within each symmetry, here we plot the $g(r)$ for all precursor particles. For comparison, we also plot the $g(r)$ for normal ($T > T_m$) and supercooled ($T < T_m$) liquids. All plots indicate amorphous structures at the bulk level.

One important question remains to be answered: by splitting the 13-neighbor particles into 12-neighbor and 14-neighbor branches, does the new approach artificially add order? The best way to address this question is to analyze a completely amorphous structure with both methods, and compare their results. We analyze the completely amorphous structure,

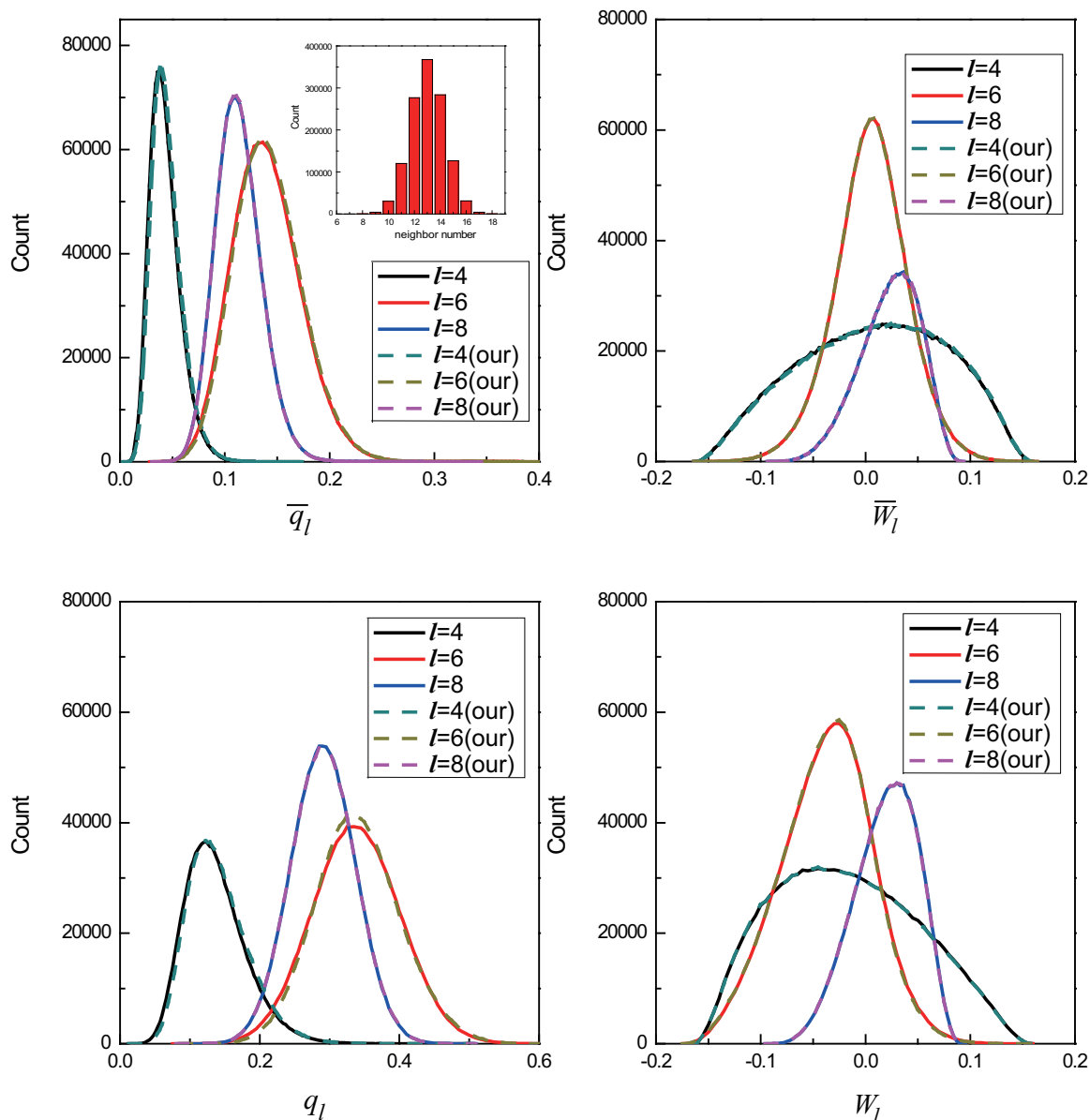


FIG. SI- 10: **A quantitative analysis on normal liquid ($T > T_m$) with two methods.** The solid lines are from the previous method, and the dashed lines are from our approach. The comparison demonstrates very little difference between the two approaches, confirming that the two methods are almost identical for a truly amorphous structure.

i.e. the normal liquid at $T > T_m$, with the two approaches. The coarse-grained bond order parameters, \bar{q}_l , \bar{W}_l , and the local bond order parameters, q_l , W_l , are plotted in Fig.SI-10. The solid lines are from the previous method, and the dashed lines are from our approach. The comparison demonstrates very little difference between the two approaches, confirming

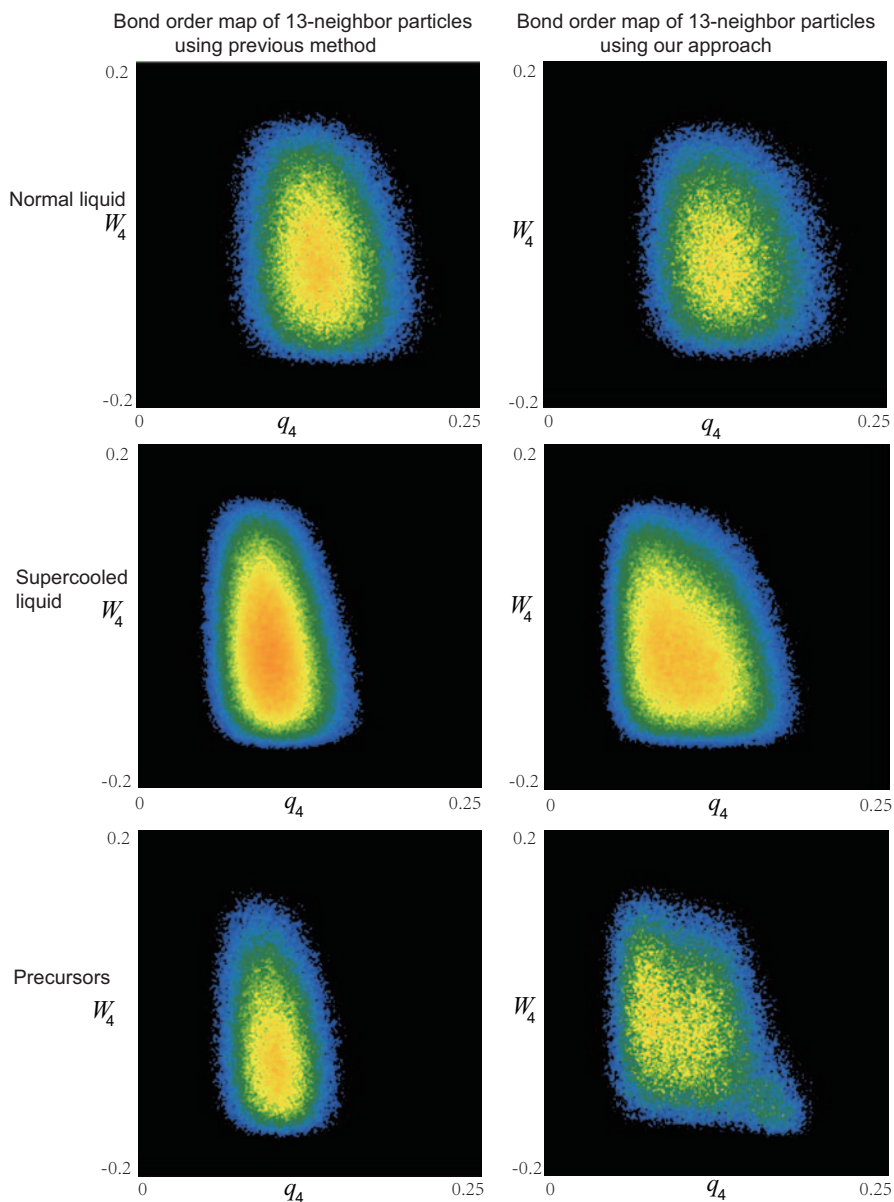


FIG. SI- 11: **Comparison of analysis on 13-neighbor particles between two methods.** For the completely amorphous normal liquid (the 1st row), the two approaches give very similar results, with no clear sign of artificially enhanced order in the new method. For the supercooled liquid (the 2nd row), a little bit of symmetry differentiation starts to emerge in our approach; while the old method can not find any clue. When the precursors are analyzed (the 3rd row), our approach clearly reveals different symmetries; but the old method fails to do that.

that the two methods are almost identical for a truly amorphous structure, with no or very little artificially added order in the new method.

To make a more clear distinction between our method and the previous method, we focus on the analysis of 13-neighbor particles, since the 12 and 14-neighbor particles are analyzed identically in both methods. We analyze the 13-neighbor particles in normal liquid at $T > T_m$, supercooled liquid at $T < T_m$ and precursors with the two approaches, and make careful comparison in Fig.SI-11. For the completely amorphous normal liquid in the 1st row, the two approaches give very similar results, with no clear sign of artificially enhanced order in the new method. In the 2nd row of supercooled liquid, a little bit of symmetry differentiation starts to emerge in our approach; while the old method can not find any clue. When the precursors are analyzed in the 3rd row, our approach clearly reveals different symmetries; but the old method fails to do that. As confirmed by the real-space arrangement in Fig.SI-4C, these local orders indeed correspond to the crystalline-symmetries, instead of artificially added by our approach. Therefore, we conclude that our approach and the old method are quite similar for the analysis of truly amorphous structures (i.e., amorphous in both short, medium, and bulk ranges); however, our method is particularly good at identifying the short-ranged order, while the previous method is not able to do that.

III. Kinetic Pathways in Hard-Sphere Systems

In hard-sphere systems, the dominant meta-stable solid is RHCP instead of BCC. Therefore, we measure the kinetic pathways in this situation and compare with the soft-repulsive systems in the main text. To prepare hard-sphere systems, we suspend PMMA particles in the mixture of cis-decahydronaphthalene and cyclohexylbromide, which matches both the density and the refractive index of particles. We dissolve the salt tetrabutylammonium chloride at the saturate concentration, which effectively screens the electric repulsion. The volume fraction of particles is around 53%. The time evolutions of relative fractions for different symmetries are shown in Fig.SI-12, for both precursors (open symbols) and nuclei (close symbols). Once again we find that the HCP-like precursor curve is above the HCP nuclei curve, while the opposite is true for BCC and FCC symmetries. This suggests kinetic pathways from HCP-like precursors to BCC and FCC solids, which is the same as the soft-potential systems. However, a main difference also exists: the major pathway is now towards the FCC nuclei, instead of BCC. Since FCC is an important component of the RHCP structure, the data again verify that the major pathway may lead to the dominant

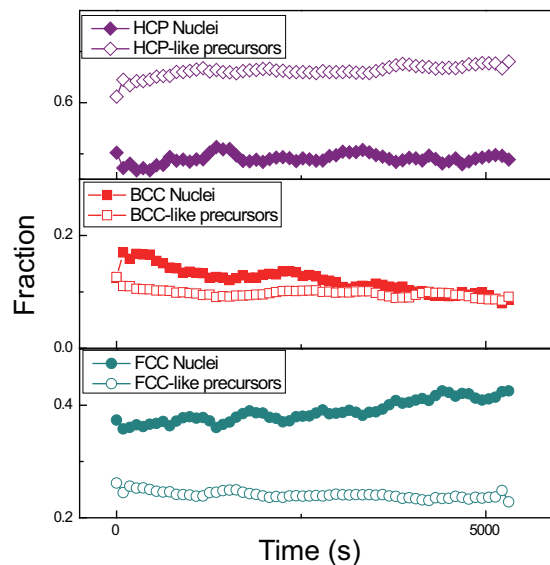


FIG. SI- 12: **Kinetic pathways in a typical hard-sphere system.** The HCP-like precursor curve is above the nuclei one; while the opposite is true for BCC and FCC symmetries. This indicates two kinetic pathways from HCP-like precursors to (1) FCC and (2) BCC nuclei. The same results are also found in the soft-potential systems shown in the main text. However, here the major pathway is towards the FCC nuclei instead of BCC, as indicated by the much larger gap in the FCC panel than in the BCC panel. This major pathway should lead to the large amount of FCC structures required by the dominant RHCP meta-stable solid. The critical nuclei size is reached around $t = 4760s$.

meta-stable solid, consistent with the finding in soft-repulsive systems.

IV. Movies

movie S1: Precursor mediated crystallization. The dark-brown spheres represent nuclei particles, the light-brown spheres indicate precursors, and the blue dots are liquid particles.

movie S2: Symmetry transformations for precursors and nuclei during crystallization. The three symmetries are represented by three colors: HCP nuclei + HCP-like precursors (purple spheres), BCC nuclei + BCC-like precursors (red spheres), and FCC nuclei + FCC-like precursors (green spheres).

movie S3: Symmetry transformations for nuclei only. The three symmetries are repre-

sented by three colors: HCP nuclei (purple spheres), BCC nuclei (red spheres), and FCC nuclei (green spheres).

-
- [1] Yethiraj, A. & Blaaderen, A. V. A colloidal model system with an interaction tunable from hard sphere to soft and dipolar. *Nature* **421**, 513-517 (2003).
 - [2] Leunissen, M. E. *et al.* Ionic colloidal crystals of oppositely charged particles. *Nature* **437**, 235-240 (2005).
 - [3] Tan, P., Xu, N., Schofield, A. & Xu, L. Understanding the Low-Frequency Quasilocalized Modes in Disordered Colloidal Systems. *Phys. Rev. Lett.* **108**, 095501 (2012).
 - [4] Hynninen, A. & Dijkstra, M. Phase diagrams of hard-core repulsive Yukawa particles. *Phys. Rev. E* **68**, 021407 (2003).
 - [5] Maxwell-Garnett, J. C. *Philos. Trans. R. Soc. London, Ser. A*, **203**, 385, (1904).
 - [6] Walden, P. *Z. Phys. Chem* **55**, 207 (1906).
 - [7] Walden, P. *Z. Phys. Chem.* **55**, 246 (1906).
 - [8] Royall, C. P., Leunissen, M. E. and van Blaaderen, A. *J. Phys. Condens. Matter* **15**, 3581-3596 (2003).
 - [9] Carrique, F., Arroyo, F. J. & Delgado, A. V., *Journal of Colloid and Interface Science* **252**, 126 (2002).
 - [10] Loeb, A. L., Wiersema, P. H. & Overbeek, J. Th. G. *The Electrical Double Layer around a Spherical Particle*, MIT Press, Cambridge, Mass. (1961).
 - [11] Crocker J. C. & Grier, D. G. Methods of Digital Video Microscopy for Colloidal Studies. *J. Colloid Interface Sci.* **179**, 298 (1996).
 - [12] Meijer, E. J. & Frenkel, D. Melting line of Yukawa system by computer simulation. *J. Chem. Phys.* **94**, 2269-2271 (1991).
 - [13] Zahn, K. & Maret, G. Dynamic Criteria for Melting in Two Dimensions. *Phys. Rev. Lett.* **85**, 3656-3659 (2000).
 - [14] Steinhardt, P. J., Nelson, D. R. & Ronchetti, M. Bond-orientational order in liquids and glasses. *Phys. Rev. B* **28**, 784-805 (1983).
 - [15] ten Wolde, P., Ruiz-Montero, M. J. & Frenkel, D. Simulation of homogeneous crystal nucleation close to coexistence. *Faraday Discuss* **104**, 93-110 (1996).

- [16] Lechner, W. & Dellago, C. Crystal structures based on averaged local bond order parameters. *J. Chem. Phys.* **129**, 114707 (2008).
- [17] Russo, J. & Tanaka, H. Selection mechanism of polymorphs in the crystal nucleation of the Gaussian core model. *Soft Matter* **8**, 4206-4215 (2012).
- [18] Fillion, L., Ni, R., Frenkel, D. & Dijkstra, M. Simulation of nucleation in almost hard-sphere colloids: The discrepancy between experiment and simulation persists. *J. Chem. Phys.* **134**, 134901 (2011).
- [19] Kawasaki, T. & Tanaka, H. Formation of a crystal nucleus from liquid. *Proc. Nat. Acad. Sci.* **107**, 14036-14041 (2010).
- [20] Ogata, S. Monte Carlo simulation study of crystallization in rapidly supercooled one-component plasmas. *Phys. Rev. A* **45**, 1122 (1992).
- [21] Gasser, U., Weeks, E. R., Schofield, A., Pusey, P. N. & Weitz, D. A. Real-Space Imaging of Nucleation and Growth in Colloidal Crystallization, *Science* **292**, 258-262 (2001).
- [22] Schilling, T., Schöpe, H. J., Oettel, M., Opletal, G. & Snook, I. Precursor-Mediated Crystallization Process in Suspensions of Hard Spheres, *Phys. Rev. Lett.* **105**, 25701(2010).
- [23] Tóth, G. I., Pusztai, T., Tegze, G., Tóth, G., & Gránásy, L. Amorphous Nucleation Precursor in Highly Nonequilibrium Fluids, *Phys. Rev. Lett.* **107**, 175702 (2011).
- [24] Schöpe, H. J., Bryant, G. & van Meegen, W. Two-Step Crystallization Kinetics in Colloidal Hard-Sphere Systems, *Phys. Rev. Lett.* **96**, 175701 (2006).
- [25] Lutsko, J. F. & Nicolis, G. Theoretical Evidence for a Dense Fluid Precursor to Crystallization, *Phys. Rev. Lett.* **96**, 046102 (2006).